UNIVERSITY OF CALIFORNIA, SAN DIEGO

Lipid-polymer hybrid nanoparticles: A photoacoustic imaging tool for ovarian cancer diagnosis

A Thesis submitted in partial satisfaction of the requirements of the degree Master of Science

in

Bioengineering

by

Chien-Ju Chen

Committee in charge:

Professor Jesse V. Jokerst, Chair
Professor Sheng Zhong, Co-Chair
Professor Kun Zhang

2017

The Thesis of Chien-Ju Chen is approved and it is acceptable in quality and form for publication on microfilm and electronically:

_____

_____

Co-Chair

_____

Chair

University of California, San Diego

2017

Table of Contents

List of Figures

List of Tables

List of Schemes

ABSTRACT OF THE THESIS

Lipid-Polymer hybrid nanoparticles: photoacoustic imaging platform applied to ovarian cancer diagnosis

by

Chien-Ju Chen

Master of Science in Bioengineering

University of California, San Diego, 2017

Professor Jesse Jokerst, Chair

Professor Sheng Zhong, Co-Chair

The survival rate of patients with ovarian cancer is over 90% in Stages I and II but

detection strategies based on CA125 testing are ineffective. Hence, this screening approach not only fails to decrease ovarian cancer mortality but also causes significant harm including major surgery in cancer free women. Fortunately, the metrics of ultrasound-based techniques are encouraging—a recent large scale trial of over 200,000 women indicated that the sensitivity and specificity were 89.4% and 99.8%, respectively, when combined with CA125 tests. However, the positive predictive value of ovarian cancer was only 43.3%. Therefore, we hypothesize that using photoacoustic ultrasound combined with lipid-polymer hybrid nanoparticles can achieve advances in specificity and sensitivity that are need in population-wide studies. In our study, we used poly-lactic-co-glutamic acid (PLGA), lecithin, and 1,2-distearoyl-*sn*-glycero-3-phosphoethanolamine-N-[folate(polyethylene glycol)]-5000 (DSPE-PEG-folate) to fabricate hybrid nanoparticles. The photoacoustic imaging agents DiR or IR-1061 were encapsulated in PLGA hydrophobic core. The folate-functionalized nanoparticles can actively target HeLa cells which overexpress folate receptors on their cell membrane. The main hypothesis is that the folate-functionalized nanoparticles could produce higher contrast between ovarian cancer tissues and normal tissues than nanoparticles without folate modification. Also, we proved our IR-1061-loaded nanoparticles had a pH-responsive release profile. We can even use photoacoustic imaging to track the releasing IR-1061 in PBS at different pH values. In the future, we attempt to conjugate IR-1061 molecules with anti-cancer drugs to endow our nanoparticles theranostic capability. Our long-term goal is to achieve in vivo photoacoustic imaging and theranostic treatment of ovarian cancer patients.

Introduction

1. Tools of early ovarian cancer diagnosis

Ovarian cancer is highly curable in the first and second stage but it is rather lethal in the late stages. It is indicated that the 5-year survival rate is over 90% if the patients are diagnosed in early stages (stage I and stage II). [3]

However, traditional CA125 testing is not effective for screening potential patients with ovarian cancer and results in less than 50% of 5-year survival rate[3, 4]. Moreover, this screening method has been evaluated as D grade[5] by US Preventive Task Force recently. Fortunately, this screening method is improved when it is combined with ultrasound imaging. Recently, a research group in UK has performed UKCTOCS trial on more than 200,000 female patients using CA125 testing combined with ultrasound imaging and it showed that the sensitivity and specificity can reach 89.4% and 99.8%[6], respectively. Although CA125 testing combined with ultrasound imaging has promising sensitivity and specificity, the positive predictive value of this method is only 43.3%. The main reason of diagnosis failure is due to the weak contrast between malign tumor tissues and healthy tissues. This research study aims to use photoacoustic ultrasound and molecular imaging to overcome this problem.

Different from traditional ultrasound imaging, photoacoustic imaging utilize imaging agents accumulated in tumor tissues to create photoacoustic signals after laser irradiation. Briefly, the photoacoustic imaging agents accumulated in biological tissues absorb the laser irradiation energy and undergo thermos-elastic expansion. Then, the

thermo-elastic expansion creates pressure wave in biological tissues. The pressure wave signal is itself a sound wave signal and could be received by ultrasound transducer. So, it's a "light in" and "sound out" imaging modality. Compared to traditional ultrasound imaging, photoacoustic imaging could enhance the contrast between tumor tissues and normal tissues.

2. Molecular imaging of folate receptors on ovarian cancer cells

We make use of molecular imaging to specifically image ovarian cancer cells via over-expressed folate receptors on ovarian cancer cell membrane. However, the biggest limit to combine photoacoustic and molecular imaging is the lack of appropriate imaging agents. For example, microbubbles demonstrate strong ultrasound imaging when they actively target to endothelial cells in vasculature. Nonetheless, microbubbles suffer from short half-time and their large sizes prevent them from passing blood vessels and targeting the folate receptors on ovarian cancer cells[1, 7]. Hence, in this study, we developed dye-loaded nanoparticles as photoacoustic imaging agents. Other research groups have developed a series of nanoparticle-based imaging agents[8-12] applied to ultrasound imaging to overcome the disadvantages of microbubbles used in ovarian cancer in vivo imaging[1, 2].

3. Photoacoustic imaging agents

Light and imaging fluorophores have been profoundly used in clinical practice and scientific research[13, 14]. Since photoacoustic imaging relies on laser irradiation to produce signals, proper usage of light and fluorophores is critical. To promote the practical use in in vivo biomedical imaging, near-infrared I (NIR I, 750-900 nm) and near-infrared II (NIR II, 1000-1700 nm) fluorophores are selected because of less auto-fluorescence disturbance, deep tissue penetration, and less photon scattering[14-18].

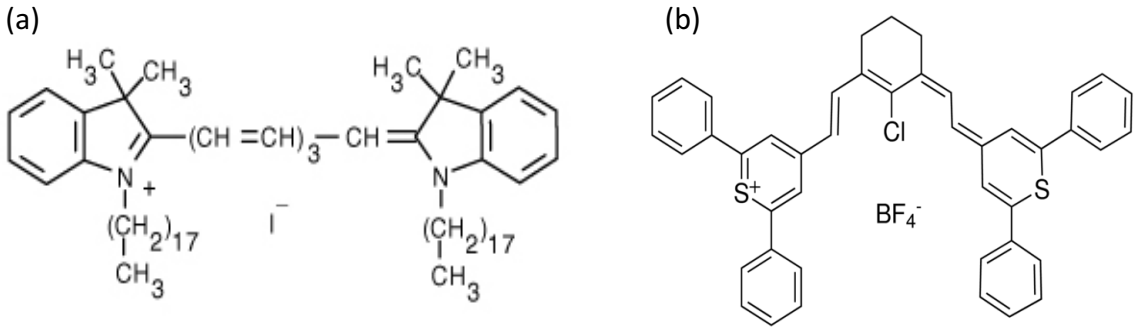

Figure 1: Chemical structure of photoacoustic imaging agents. (a) DiR (b) IR-1061.

In this study, we select DiR and IR-1061 as our photoacoustic imaging agents. DiR has absorbance peak at 765 nm while IR-1061 has absorbance peak at 1074 nm. So, both imaging agents are either NIR fluorophores. DiR is a hydrophobic fluorophore and has longer fluorescence lifetime than other hydrophilic fluorophores Cy5 and Cy7[19] and high quantum yield. It has been successfully applied to improved fluorescence in vivo imaging[19]. The hydrophobic property of DiR make it compatible to our lipid-polymer hybrid nanoparticles and could give rise to higher loading efficiency. Similarly, IR-1061 is hydrophobic and could also lead to high dye loading efficiency. Moreover, IR-PEG nanoparticles loaded with IR-1061 has been developed by another research group. This

IR-PEG nanoparticle successfully provided enhanced resolution in in vivo fluorescence imaging in mice because of its' longer emission wavelength over 1000 nm[20]. However, the quantum yield of IR-1061 is only 1.8%, which causes low fluorescence intensity and hinders its' further use in biological imaging of deeper tissues. Although the low quantum yield of IR-1061 lowers down the signal intensity in fluorescence imaging, it may convert more laser irradiation energy to heat, which promotes thermos-elastic expansion in biological tissues and improves photoacoustic signals.

Results

1. Spectral Properties of free DiR and IR-1061:

The absorbance spectra of DiR molecules dissolved in acetonitrile was shown in Figure 2 (a). It showed an absorbance peak at 765 nm. Also, the absorbance of DiR illustrated a concentration-dependent increasing tendency. The absorbance of DiR at different concentrations were taken to do a linear regression and obtained a standard line. It turns out that the DiR concentrations and the absorbance show remarkably linear tendency with R^2>0.99 (Figure 2 (b)). We used this standard line combined with the absorbance of destroyed DiR-loaded hybrid nanoparticles to quantify the loading efficiency of DiR.

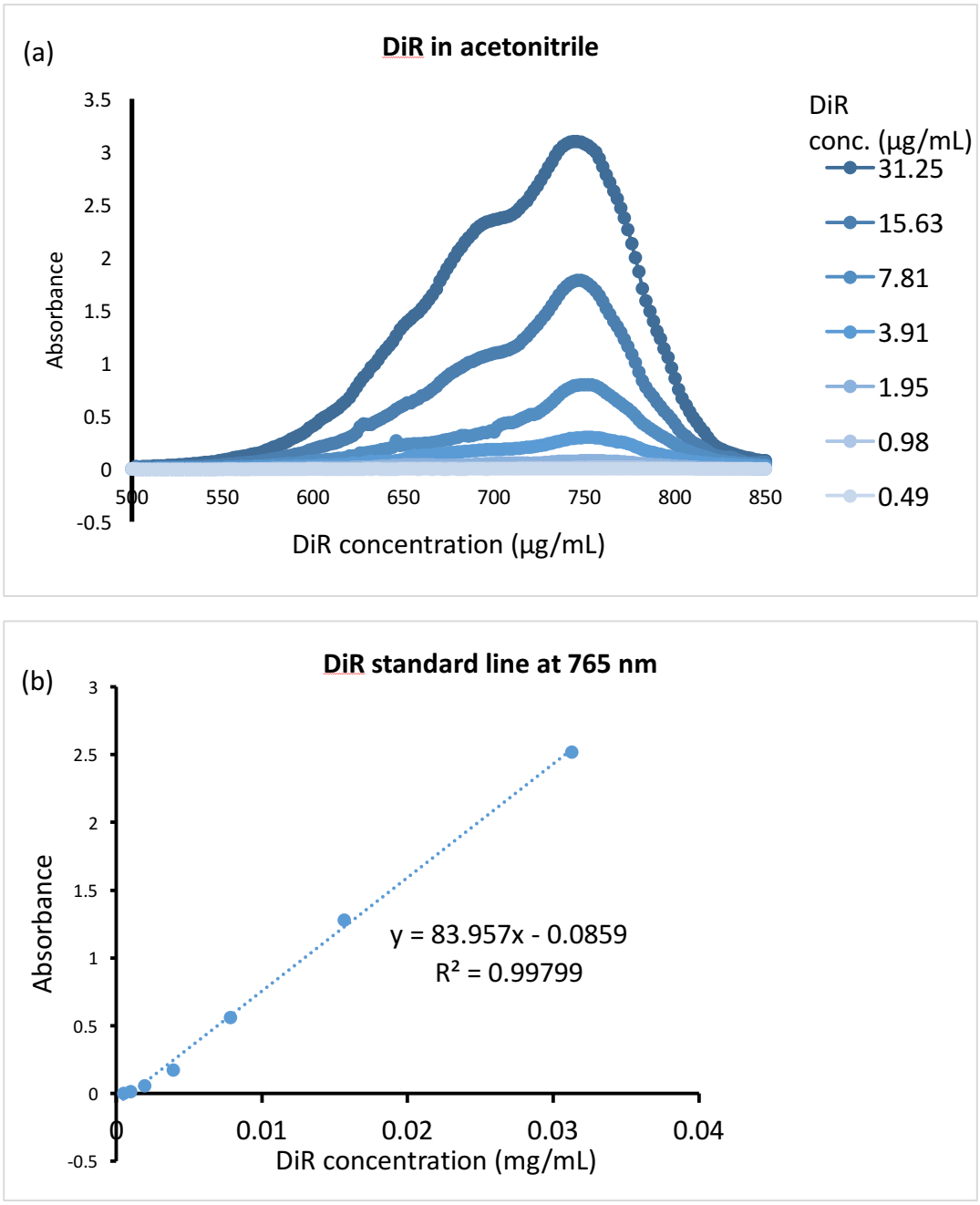

Figure 2: **Spectral properties of DiR** (a) UV/Vis absorbance spectra (500-850 nm) of free DiR molecules in acetonitrile at different concentrations. (b) Standard line of free DiR molecules in acetonitrile at 765 nm.

Similarly, IR-1061 molecules were dissolved in DMSO and the absorbance spectra were obtained by using UV/Vis/NIR spectrophotometer. Free IR-1061 in DMSO showed a pronounced absorbance peak at 1074 nm with a shoulder peak at 945 nm (Figure 3 (a)). We used the absorbance of IR-1061 at 945 nm and 1074 nm to obtain the standard lines. It illustrated that the standard line at either wavelength have remarkable linear tendency with $R^2 > 0.999$ (Figure 3 (b)). The standard line at 1074 nm was used to quantify the encapsulated IR-1061 in hybrid nanoparticles after the nanoparticles were destroyed with DMSO.

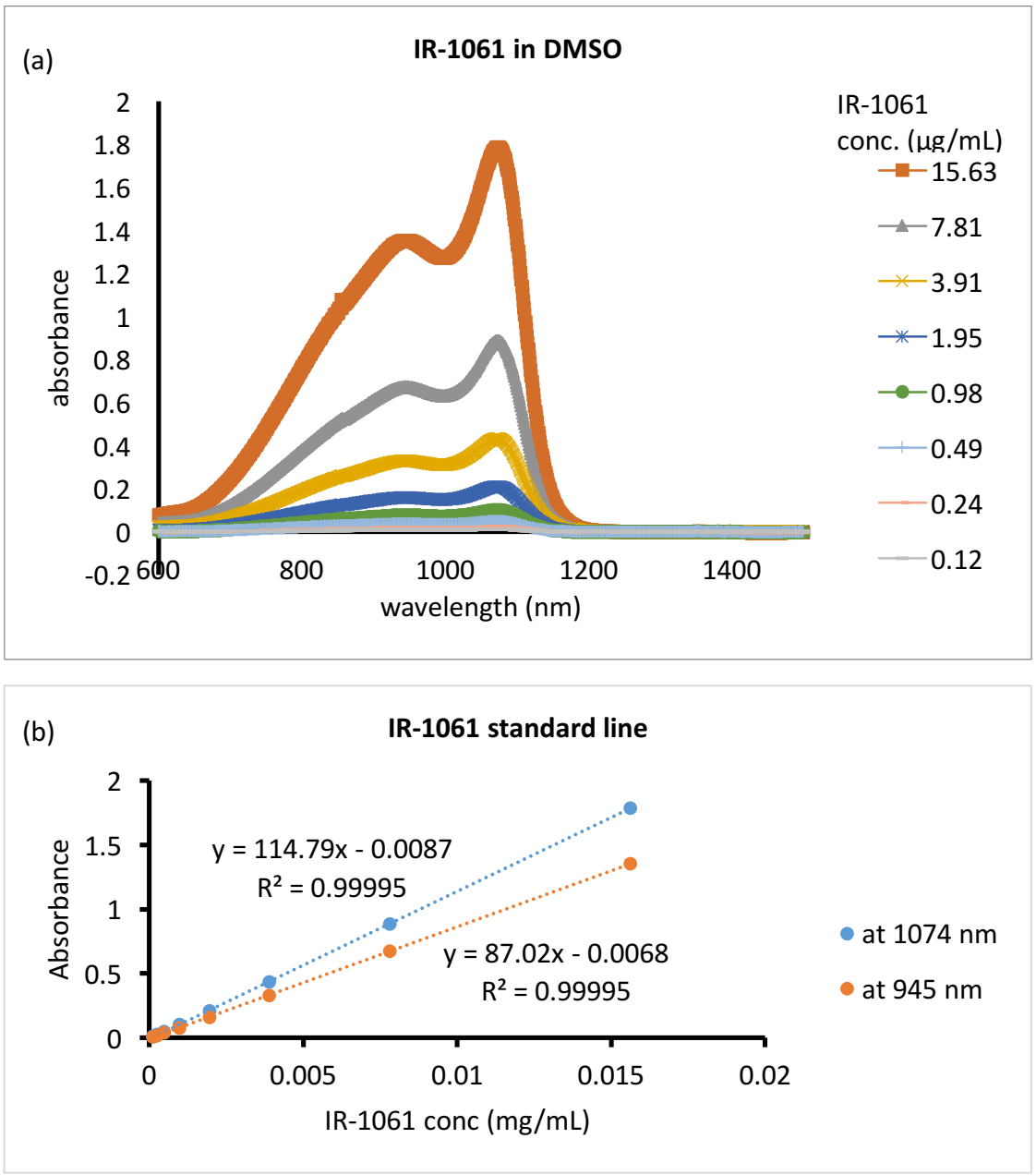

Figure 3: Spectral properties of IR-1061. (a) UV/Vis/NIR absorbance spectra (600-1500 nm) of free IR-1061 molecules in DMSO at different concentrations. (b) Standard line of free IR-1061 molecules in DMSO at 945 and 1074 nm.

2. Characterization of Nanoparticles

(1) DiR-loaded hybrid nanoparticles:

Scheme 1: Schematic diagram of DSPE-PEG-FA and hybrid nanoparticles. (a) The chemical structure of DSPE-PEG-FA was demonstrated. The folate molecule was shown as red motif and PEG polymer was shown as black curl. The DSPE phospholipid was draw as green hydrophilic head and two black hydrophobic tails. (b) The hybrid nanoparticles were made by nanoprecipitation method.

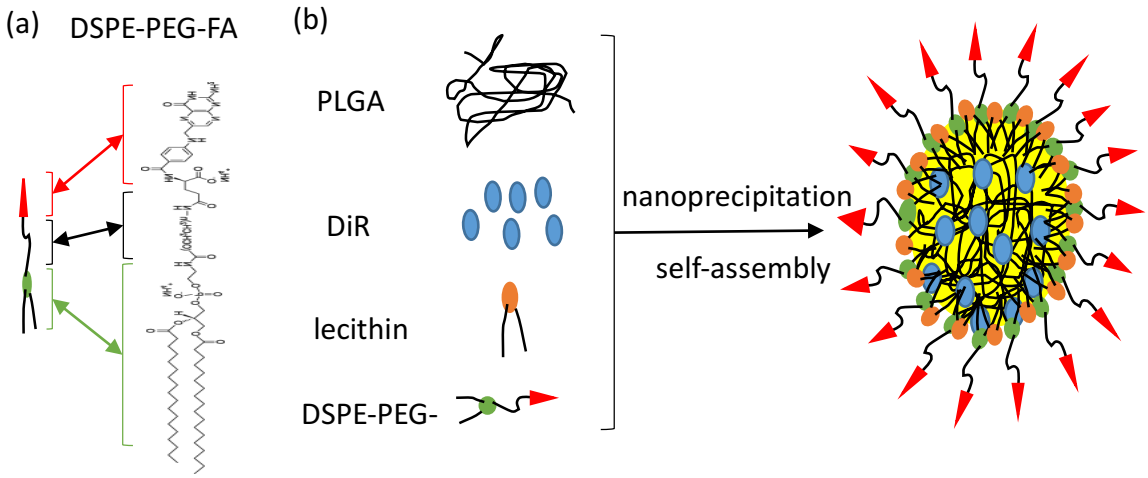

The DiR-loaded hybrid nanoparticles were prepared by nanoprecipitation method. As depicted in Scheme 1, the PLGA polymer matrix and DiR molecules formed hydrophobic cores and the hydrophobic tails of lecithin and DSPE-PEG-FA molecules were intercalated into the hydrophobic cores via hydrophobic interactions. Then, the hydrophilic heads of lecithin and DSPE-PEG-FA molecules formed hydrophilic shells to stabilize hybrid nanoparticles in aqueous phase. Table 1 summarized the size, PDI, zeta-potential, and loading efficiency of DiR. We compared the properties of hybrid nanoparticles without any cargos and PLGA nanoparticles. It illustrated in Figure 4 (a) that hybrid nanoparticles were one and a half times bigger than PLGA particles. This may be due to the additional lecithin and DSPE-PEG shell which enlarges the average size of

hybrid nanoparticles. Also, after adding the lipid shell, the zeta-potential became slightly more positively charged (from -33.1 mV to -29.8 mV). This may be due to the fact that PEG layer moderately shells the negatively charged PLGA hydrophobic core. After DiR molecules were encapsulated into the hybrid nanoparticles, the average size of the hybrid nanoparticles become even bigger because of the extra DiR molecules loaded into the hydrophobic core. Similarly, folate-functionalized nanoparticles had the largest average size which is due to the additional folate layer. Also, we found the size distribution of DiR-loaded nanoparticles with or without folate were similar except a second peak in the folate-functionalized nanoparticles with DiR (Figure 4(b)). The second peak may result from slightly aggregation of folate-functionalized nanoparticles with DiR and higher up the value of average size. After DiR-loaded hybrid nanoparticles were destroyed by acetonitrile, the absorbance was measured. Combined with the DiR standard line (Figure 2 (b)), we obtained the loading efficiency of hybrid nanoparticles with and without folate modification was 74.8% and 70.1%, respectively. The loading efficiency of the hybrid nanoparticles is so high. This may because the lipid monolayer at the interface of PLGA hydrophobic core prevents DiR molecules from diffusing out of nanoparticles[21].

Table 1: Characterization of hybrid nanoparticles and PLGA nanoparticles. The average size, PDI, and zeta-potential of hybrid NP w/DiR/FA, hybrid NP w/DiR, hybrid NP w/o DiR, and PLGA NP were measured by DLS. The loading efficiency of all samples was calculated using standard line in Figure 2 (b).

sample	Average size (nm)	PDI	Zeta-potential (mV)	Loading efficiency (%)
Hybrid NP w/DiR/FA	211.8±42.8	0.233	-26.0±6.6	74.8±11.9
Hybrid NP w/DiR	174.5±12.5	0.151	-29.0±3.2	70.1±6.8
Hybrid NP w/o DiR	65.8±0.3	0.425	-29.8	/
PLGA NP	45.7±0.5	0.187	-33.1	/

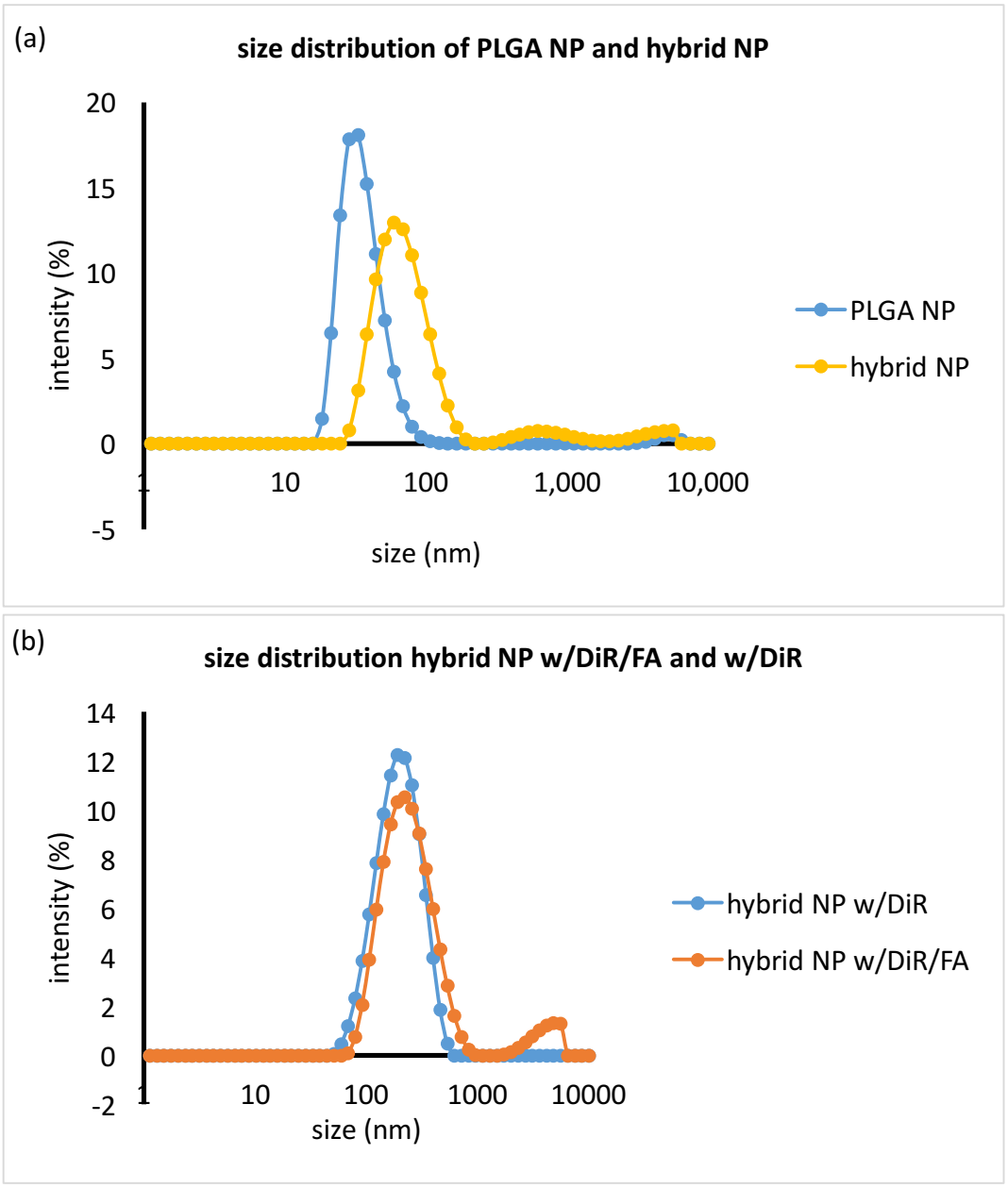

Figure 4: Size distribution of DiR-loaded hybrid nanoparticles and PLGA nanoparticles. PLGA NP, hybrid NP, hybrid NP w/DiR, and hybrid NP w/DiR/FA were prepared by nanoprecipitation method. The size distribution of all samples was examined by DLS.

(2) IR-1061-loaded hybrid nanoparticles:

We prepared the nanoparticles by a modified nanoprecipitation method[20]. The effect of different weight ratio of PLGA and IR-161 was studied. Table 2 and Table 3 summarize the size, PDI, zeta-potential, and loading efficiency of IR-1061 of nanoparticles with PLGA weight ratio of 05 and 10, respectively. We found that the nanoparticles with higher weight ratio of PLGA generally have larger size. For example, the nanoparticles with PLGA weight ratio of 05 often have the size around 110 nm while those with PLGA weight ratio of 10 usually have the size over 120 nm. Also, it is indicated in Figure 5 (a) and (c) that the size of nanoparticles did not significantly increase if we higher up the weight ratio of IR-1061. However, the zeta-potential of the nanoparticles dramatically shifted from -36 mV to around -20 mV as shown in Figure 5 (b) and (d). The loading efficiency of IR-1061 remarkably increased with higher weight ratio of IR-1061. This may result from the hydrophobic and positively charged properties of IR-1061 molecules. It is well-known that PLGA core is hydrophobic and negatively charged. Hence, IR-1061 molecules could be trapped in the PLGA core via both hydrophobic interactions and electrostatic interactions. Due to the bigger average size and higher loading efficiency of nanoparticles with weight ratio of PLGA/lipid/IR-1061 as 10/20/3.0, we made use of this nanoparticle for the following cytotoxicity and release experiments.

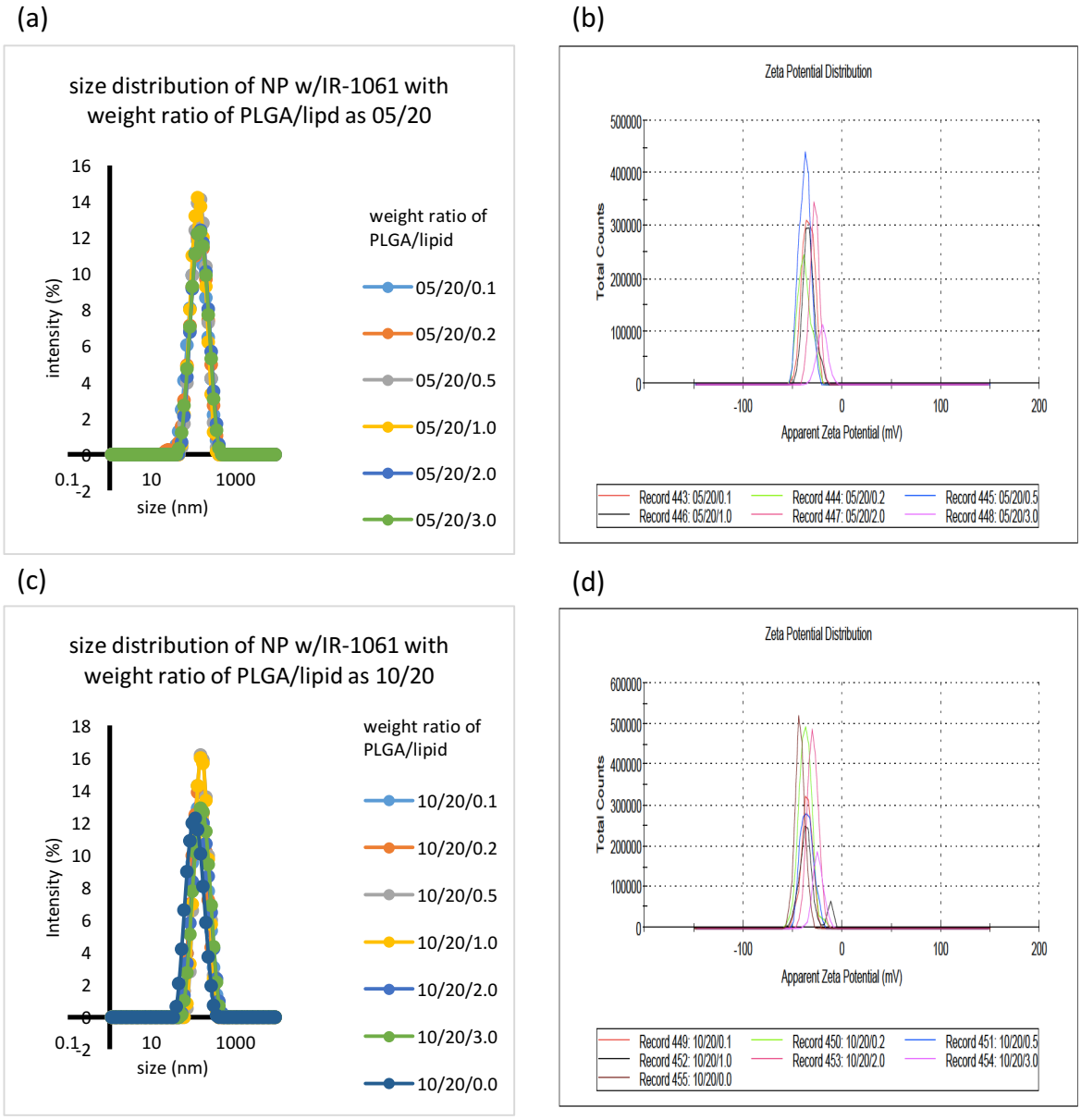

Figure 5: Size and zeta-potential distribution of IR-1061-loaded hybrid nanoparticles. The IR-1061-loaded nanoparticles were prepared by nanoprecipitation method. The size distribution and zeta-potential were examined by DLS.

Table 2: Characterization of IR-1061-loaded hybrid nanoparticles with weight ratio of PLGA to lipid as 05 to 20.

Weight ratio of PLGA/lipid/IR-1061	Average size (nm)	PDI	Z-potential (mV)	Loading Efficiency (%)
05/20/0.1	106.2±1.3	0.215	-36.2±1.6	6.1
05/20/0.2	113.0±1.4	0.208	-37.1±0.9	8.1
05/20/0.5	114.6±1.7	0.199	-37.4±0.5	33.0
05/20/1.0	110.9±1.4	0.201	-32.8±0.9	48.5
05/20/2.0	116.9±0.2	0.246	-28.3±0.5	65.5
05/20/3.0	106.3±0.7	0.262	-20.0±0.4	73.0

Table 3: Characterization of IR-1061-loaded polymeric liposome with weight ratio of PLGA to lipid as 10 to 20.

Weight ratio of PLGA/lipid/IR-1061	Average size (nm)	PDI	Z-potential (mV)	Loading Efficiency (%)
10/20/0.1	120.8±2.2	0.202	-36.1±1.5	6.2
10/20/0.2	118.7±1.3	0.181	-37.0±0.5	10.6
10/20/0.5	137.4±2.7	0.164	-36.0±1.0	19.7
10/20/1.0	130.4±1.5	0.189	-34.9±0.5	32.4
10/20/2.0	127.2±2.0	0.222	-29.8±0.5	59.1
10/20/3.0	126.7±1.3	0.229	-23.8±0.8	67.8
10/20/0.0	90.1±1.1	0.221	-41.9±1.2	0

Figure 6 shows transmission electron microscopy of IR-1061-loaded hybrid nanoparticles with weight ratio of PLGA/lipid/IR-1061 as 10/20/3.0. In Figure 6 (a), we found the size of our nanoparticles were not homogeneous. For example, the small nanoparticles could be as small as 50 nm and the large ones could be around 150 nm. This gives rise to their higher PDI value (0.229) shown in Table 3. Even though the size of our nanoparticles were not ideally homogenous, the morphology of almost all nanoparticles was in sphere shape. Besides, the lipid-polymer interface was obviously sharp as shown in Figure 6 (b).

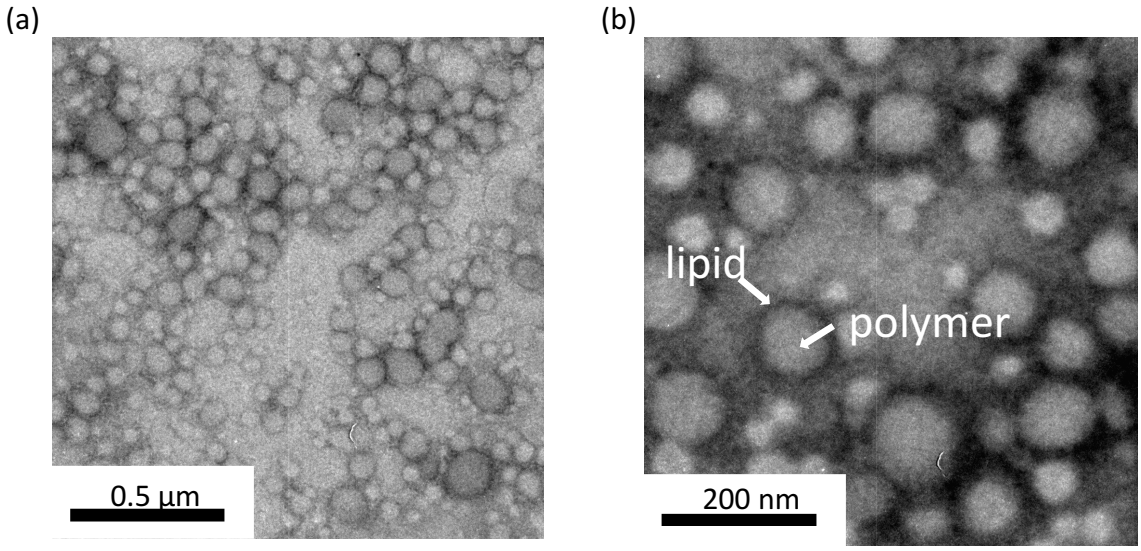

Figure 6: Transmission electron microscopy (TEM) image of IR-1061-loaded hybrid nanoparticles at different magnifications. (a) 4000X (b) 10000X.

(3) Spectral properties of IR-1061-loaded hybrid nanoparticles:

The absorbance spectra of IR-1061-loaded hybrid nanoparticles was demonstrated in figure 6. It showed an absorbance peak at 900 nm and a shoulder peak at 1087 nm. The spectral properties of IR-1061 are dramatically different between in hybrid nanoparticles (Figure 7 (a)) and in DMSO (Figure 3(a) and Figure 7 (b)). As we can see, when IR-1061 molecules are encapsulated into nanoparticles, the spectral property shows an obvious blue shift. This may results from the aggregation of IR-1061 molecules in the PLGA hydrophobic core. However, when the IR-1061-loaded nanoparticles were destroyed by DMSO, the absorbance spectral properties were restored (Figure 7 (b)). We also destroyed nanoparticles without loading any IR-1061 and no absorbance peak show in this group (10/20/0.0 in Figure 7 (b)). This result further confirm the absorbance peaks stem from IR-1061 molecules inside nanoparticles. Therefore, we expect that we can utilize the blue shift to monitor the release profile of anticancer drugs when IR-1061 molecules are conjugated with anticancer drugs. Specifically, when the IR-1061-drug conjugates are encapsulated in nanoparticles, we observe a main absorbance peak at 900 nm. After the IR-1061-drug conjugates are released, the absorbance peak should shift from 900 nm to 1074 nm. Also, when time goes on, higher amount of releasing IR-1061-drug conjugates will lead to higher absorbance and stronger photoacoustic signals.

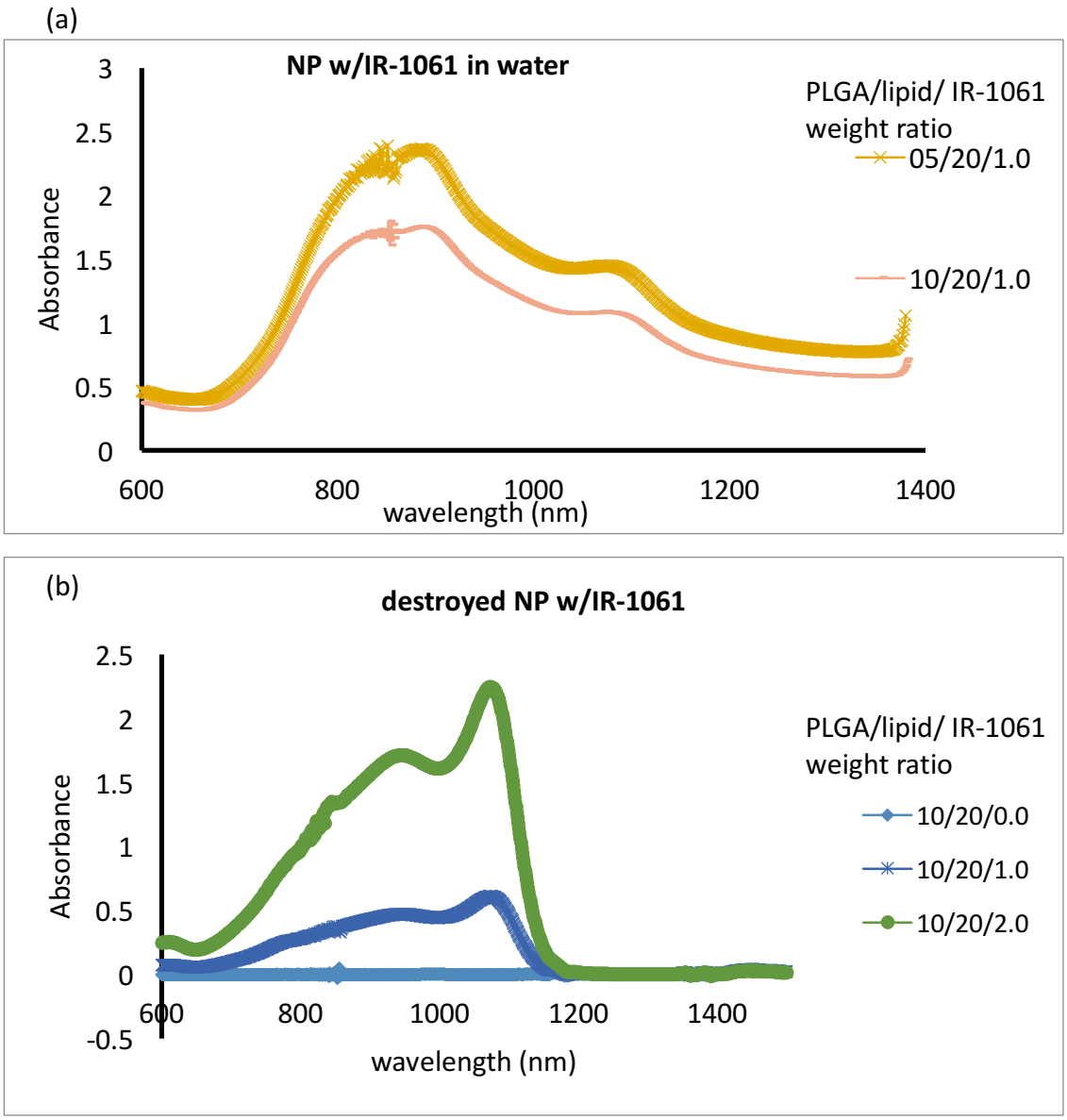

Figure 7: Spectral properties of IR-1061-loaded hybrid nanoparticles. (a) UV/Vis/NIR absorbance spectra (600-1400 nm) of IR-1061-loaded hybrid nanoparticles in Millipore water. (b) UV/Vis/NIR absorbance spectra (600-1500 nm) of destroyed IR-1061-loaded hybrid nanoparticles in DMSO.

3. Cell experiments

(1) folate receptor on A549, HeLa, and SKOV3 cells:

To choose optimal cell lines to confirm the active targeting capability of our nanoparticles, we utilize anti-folate receptor antibodies to stain folate receptors on the cell membrane of A549, HeLa, Ov2008, and SKOV3 cells. The results are shown in Figure 8. It was obvious that A549 cells had deficient expression of folate receptors since the FITC intensity was only 1.1 times higher than its' control group. In contrast, HeLa cells pronouncedly overexpressed folate receptors on their cell membrane because the FITC intensity was 7.1 times higher than its' control group. Besides, our ovarian cancer cell lines, Ov2008 and SKOV3, only moderately overexpressed folate receptors. Their FITC intensity was only 1.4 and 1.7 times higher than their control group, respectively. Hence, we chose A549 and HeLa cells as our negative and positive cell lines, respectively, for folate receptor expression to ideally validate active targeting capability of our folate-functionalized hybrid nanoparticles with DiR.

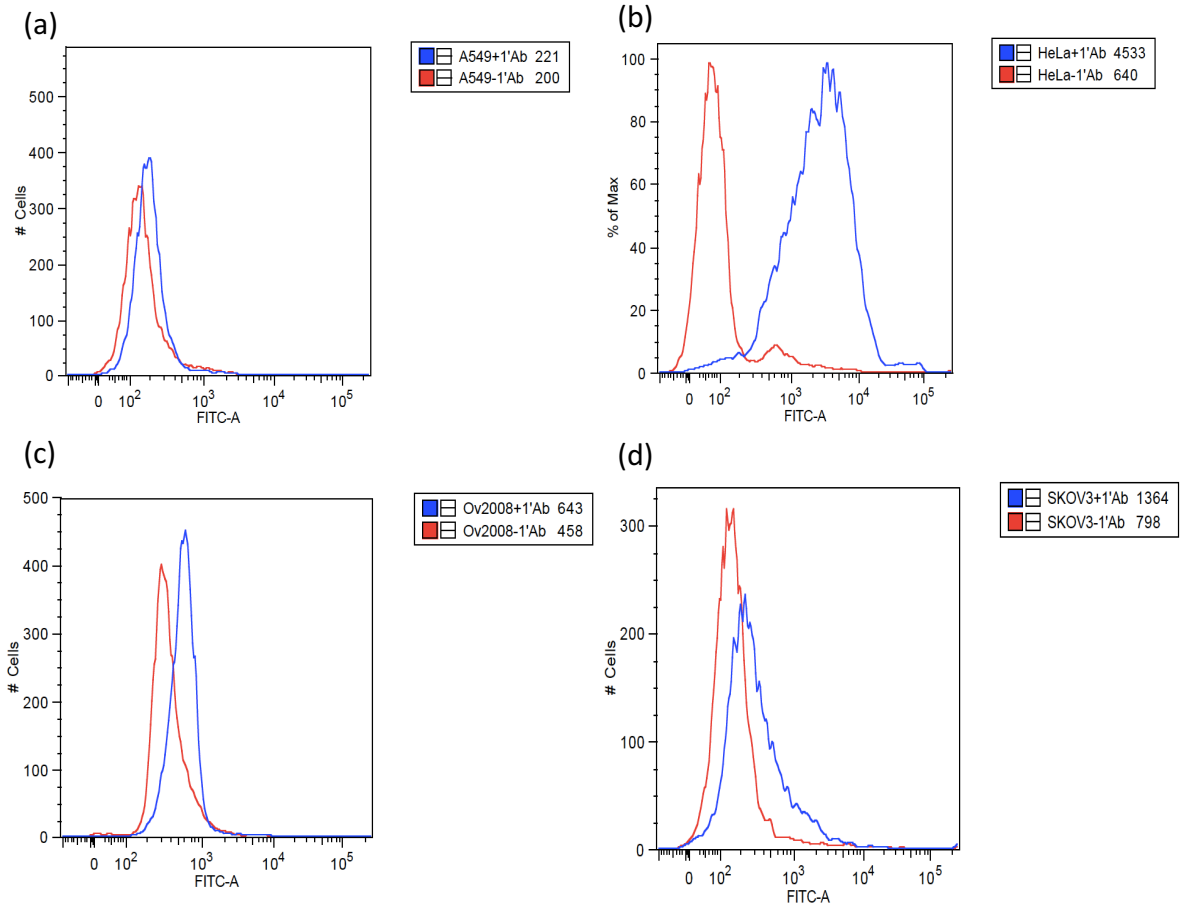

Figure 8: Folate receptors on A549, HeLa, Ov2008, and SKOV3. We immune-stained folate receptor on (a) A549, (b) HeLa, (c) Ov2008, and (d) SKOV3 cells and used flow cytometer combined with FITC-channel to examine the fluorescent intensity of cancer cells. The x-axis represents the fluorescent intensity while y-axis represents cell counts. The red line in every panel represents cells stained without primary antibodies while blue line represents cells stained with primary antibodies. All cell lines were further stained with FITC-conjugated secondary antibodies.

(2) cell uptake

To validate the active targeting capability of folate-functionalized hybrid nanoparticles, we treated HeLa and A549 cells with folate-functionalized hybrid nanoparticles loaded with DiR. Also, we treat these two cell lines with DiR-loaded nanoparticles without folate modification to compare the results. We used flow cytometer combined with APC-Cy7 channel to detect the fluorescent intensity of DiR inside cells. In Figure 9, we can see either HeLa or A549 cells had very little amount cell uptake of DiR-loaded nanoparticles without folate modification because the fluorescent intensity was almost the same as the control groups. In contrast, both cell lines had a certain level of cell uptake of folate-functionalized nanoparticles loaded with DiR in 0.5 h (Figure 9 (a)). To relatively quantify the cell uptake amount, 95% of HeLa cells engulfed a great amount of folate-functionalized nanoparticles while only 45% of A549 cells engulfed the same amount of the nanoparticles. If we prolonged the treatment time to 1h, almost all HeLa cells (97%) engulfed high amount of nanoparticles while only 49% of A549 cells engulfed the same amount of nanoparticles (Figure 9 (b)). These results confirm the active targeting capability of our folate-functionalized hybrid nanoparticles because HeLa cells which overexpressed folate receptors on their cell membrane had more cell uptake of these folate-functionalized nanoparticles than A549 cells which had deficient folate receptors.

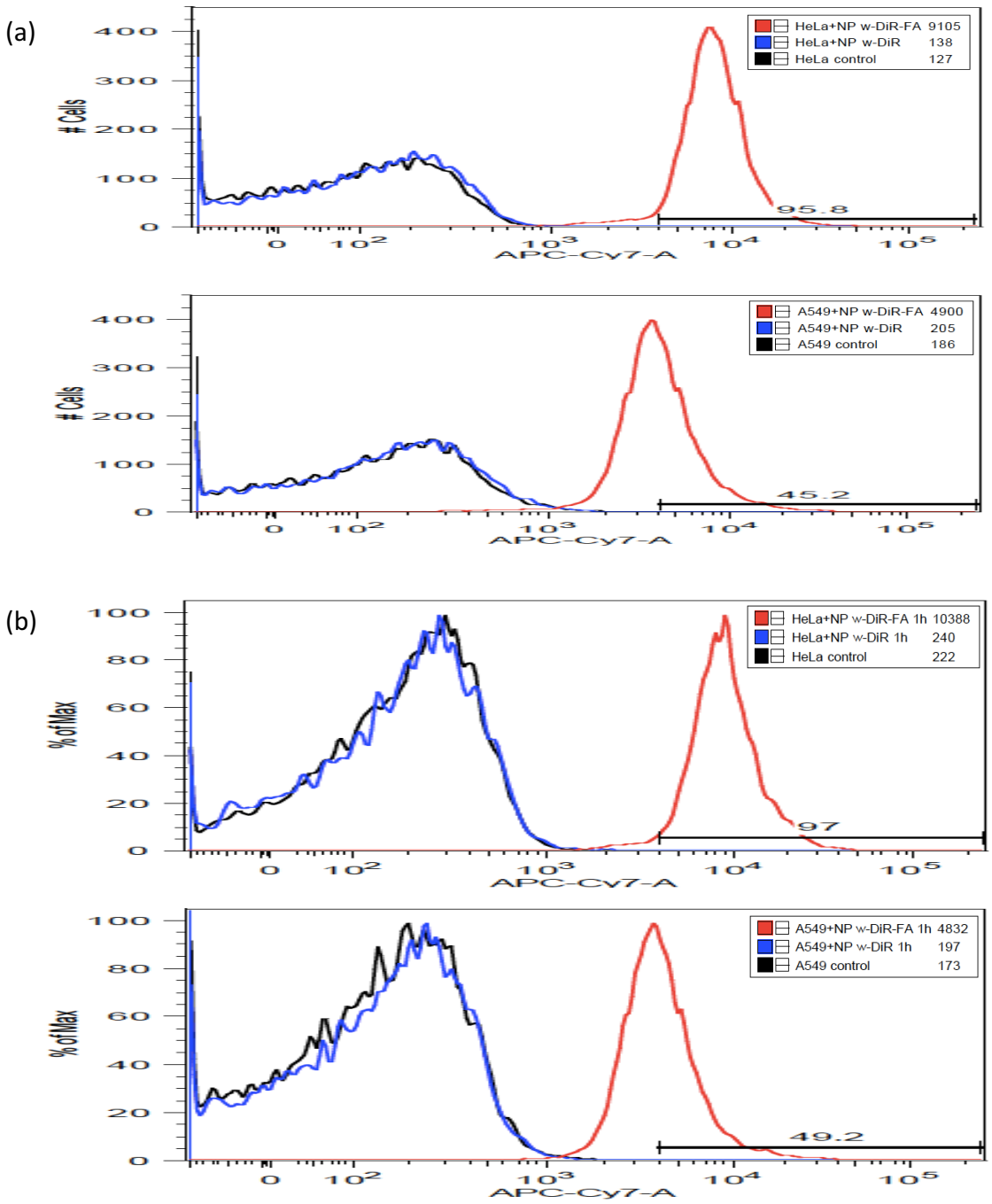

Figure 9: Flow cytometry results of HeLa and A549 cells treated with NP w/DiR/FA and NP w/DiR. HeLa cells and A549 cells were treated with NP w/ DiR (blue line) or NP w/DiR/FA (red line) for (a) 0.5h and (b) 1h. After nanoparticle treatment, all cells were washed twice by PBS. The fluorescent intensity of cells was examined by flow cytometer combined with APC-Cy7 channel.

(3) folate competition experiment:

To further confirm the active targeting capability of our folate-functionalized nanoparticles, we pretreated HeLa and A549 cells with 1, 2, and 4 mM folate for 1h and repeated the same experiment. As we can see in Figure 10, HeLa cells showed folate-dependent decreasing cell uptake of our folate-functionalized nanoparticles. In contrast, cell uptake behavior of A549 cells was almost the same no matter how much folate molecules we added beforehand. These results may be caused by the blocking of overexpressed folate receptors on HeLa cells. However, the deficient expression of folate receptors on A549 cells caused no difference of folate-functionalized nanoparticles cell uptake. All in all, these results confirm active targeting capability of our folate-functionalized hybrid nanoparticles.

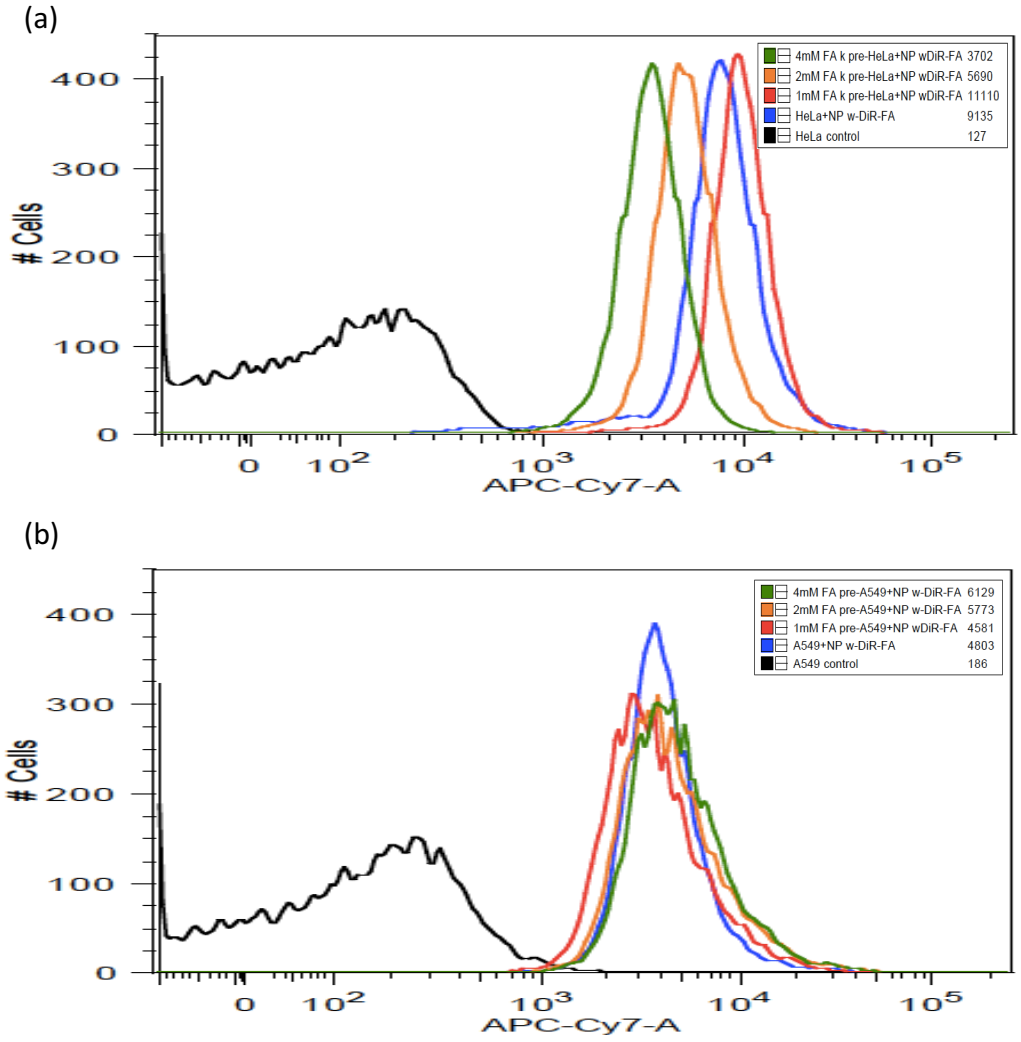

Figure 10: Flow cytometry results of HeLa and A549 cell uptake with folate pre-treatment for 1h. Then, (a) HeLa and (b) A549 cells were treated with NP w/DiR/FA for 1h. After nanoparticle treatment, all cells were washed twice by PBS. The fluorescent intensity of all cells was examined by flow cytometer combined with APC-Cy7 channel.

(4) Cell viability:

To make sure our DiR- or IR-1061-loaded hybrid nanoparticles have very little cytotoxicity, we use MTT assay to test the cell viability of HeLa and A549 cells treated with DiR- or IR-1061-loaded nanoparticles. In Figure 11, both cell lines were treated with DiR- or IR-1061-loaded nanoparticles. The cell viability of HeLa and A549 cells was over 90% even after they were treated 200 μg/mL DiR- or IR-1061-loaded nanoparticles for 4h. These results validate our DiR- or IR-1061-loaded nanoparticles have very little cytotoxicity. Since PLGA and PEG polymers were FDA approved and validated to be biocompatible, the biocompatibility of these materials gives rise to the minimal cytotoxicity of our DiR- or IR-1061-loaded hybrid nanoparticles.

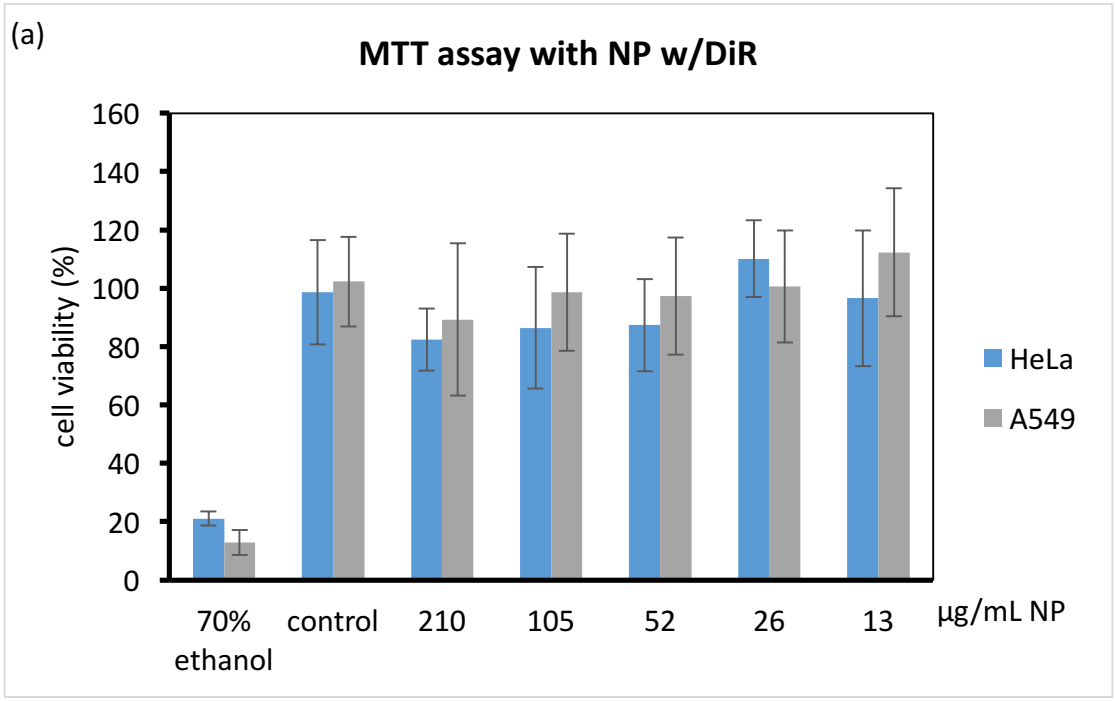

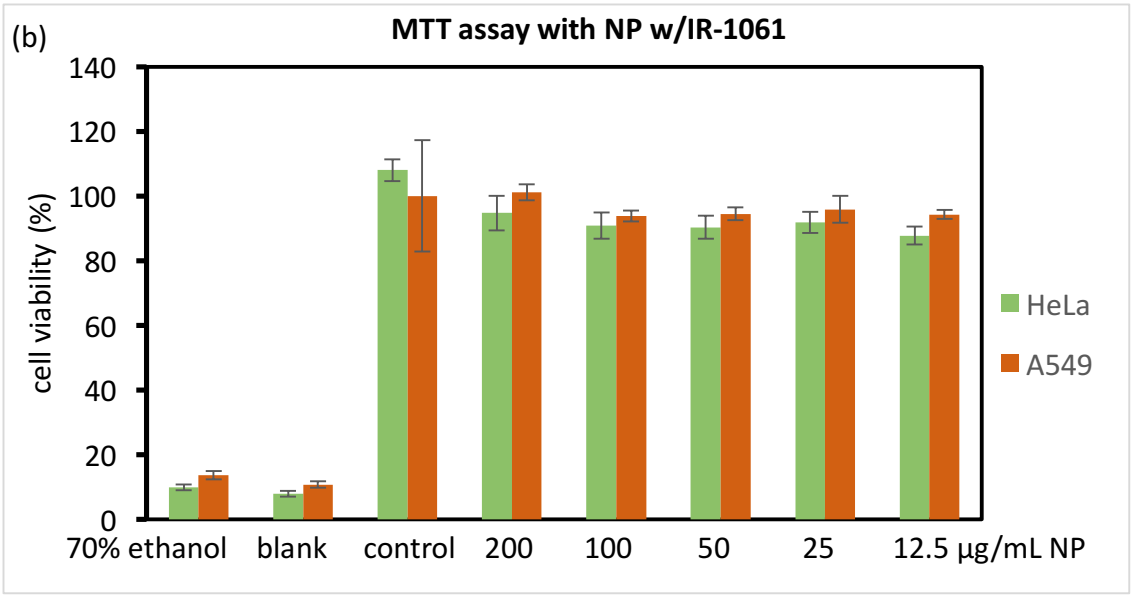

Figure 11. Cell viability of HaLa and A549 cells treated with (a) DiR and (b)IR-1061-loaded hybrid nanoparticles at different concentrations for 4h.

4. Release Profile

The release profile of IR-1061-loaded hybrid nanoparticles in PBS at pH 7.4, 6.6, 5.7, and 4.5 was illustrated in Figure 12. In all testing groups, the amount of released IR-1061 was increasing when time went on. Furthermore, the more acidic the environment, the more IR-1061 molecules were released. Again, this may be due to the positively charged nature of IR-1061 molecules. In more acidic environment, the extra protons could interact with the negatively charged PLGA core. So, the electrostatic interaction between IR-1061 and PLGA core was disturbed, which led to IR-1061 release. To confirm our hypothesis. The size, PDI, and zeta-potential of releasing samples were measured by DLS at 24h (Table 4). The size of all releasing nanoparticles had little change but the zeta-potential of zeta-potential become more positive in more acidic environment. The results further confirm our hypothesis about how IR-1061 molecules are released. However, the IR-1061-loaded nanoparticles released their IR-1061 molecules over 60 % at 96h only in PBS at pH 4.5. At pH 5.7 and 6.6, the hybrid nanoparticles slightly released IR-1061 more than 50%. At pH 7.4, the nanoparticles barely released IR-1061 molecules over 40%. This may results from the hydrophobic interaction between IR-1061 molecules and PLGA core. Specifically, although the disturbance of electrostatic interaction between IR-1061 molecules and PLGA cores. IR-1061 molecules still have some hydrophobic interactions between PLGA cores, which causes substantial release of IR-1061.

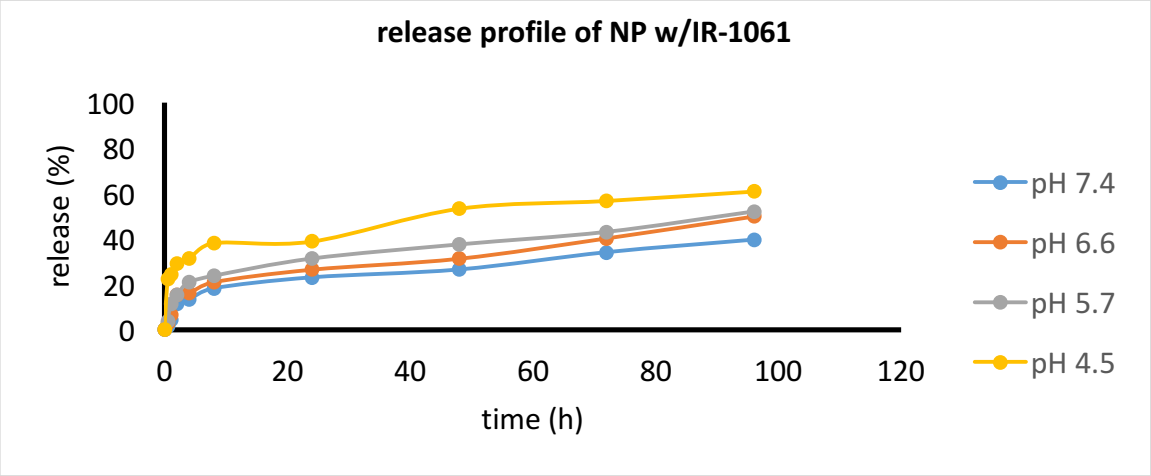

Figure 12: Release profile of IR-1061-loaded hybrid nanoparticles in PBS at pH 7.4, 6.6, 5.7, and 4.5.

Table 4. Characterization of releasing samples at 24h.

sample	Average size (nm)	PDI	zeta-potential (mV)
NP w/IR-1061	136.6	0.102	-22.2±4.2
NP release at pH 7.4	153.6	0.215	-16.8±4.2
NP release at pH 6.6	149.6	0.207	-18.2±9.4
NP release at pH 5.7	147.3	0.211	-14.8±1.3
NP release at pH 4.5	141.7	0.171	-0.8±3.4

However, we found that some aggregate appeared in our releasing samples when releasing time went up to 24h. Figure 13 shows the aggregate in our releasing samples at 72h. More aggregate showed up in releasing samples in acidic environment, especially at pH 4.5. Combined with the release profile in Figure 12, we conclude that the released IR-1061 molecules aggregate in aqueous environment due to their hydrophobicity. As a result, the greater amount of released IR-1061 molecules in PBS at pH 5.7 and 4.5 severely agglomerated and cause pronounced aggregate in PBS.

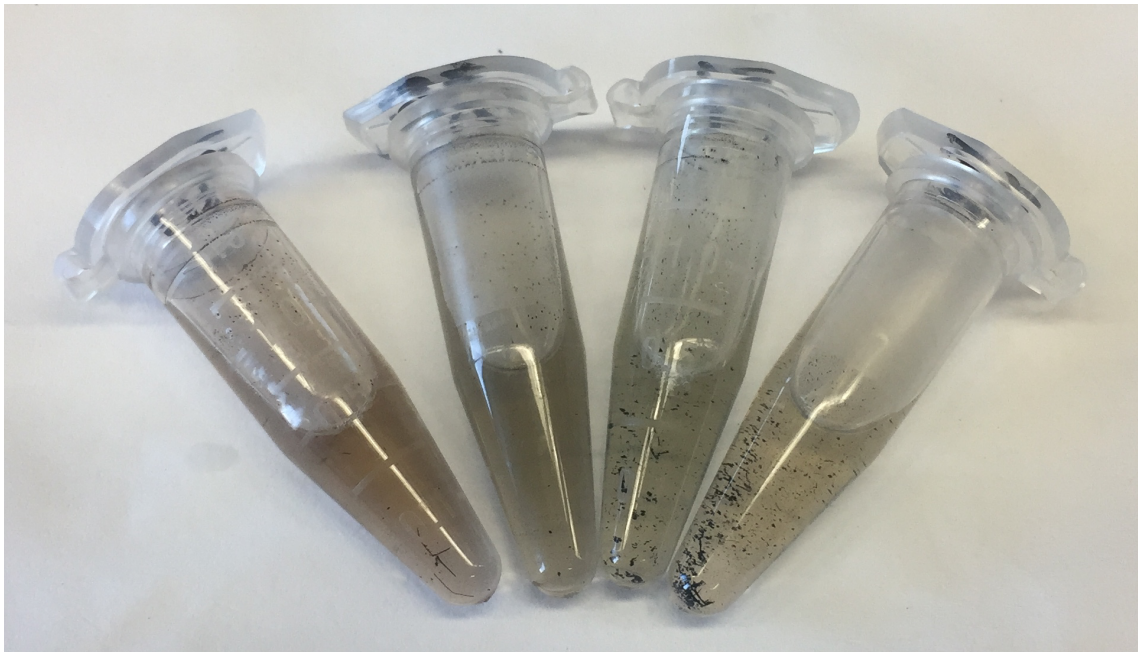

pH 7.4 pH 6.6 pH 5.7 pH 4.5

Figure 13: Releasing samples in pH 7.4, 6.6, 5.7, and 4.5 PBS at 72h.

5. Photoacoustic Imaging

(1) Detection limit of IR-1061 in DMSO:

The photoacoustic imaging of free IR-1061 dissolved in DMSO was shown in Figure 14. As we can see, the higher concentration of IR-1061, the higher the corresponding photoacoustic intensity. We used Image J to quantify the pixel intensity and found that the IR-1061 concentration-dependent increasing tendency of photoacoustic intensity (Figure 15 (a)). Furthermore, the linear regression (Figure 15 (b)) illustrated remarkable linear fit (R^2>0.95). Combined with the standard line and the mean of DMSO blank plus three standard deviation of DMSO blank, we obtained the detection limit of IR-1061 was 7.04 μM.

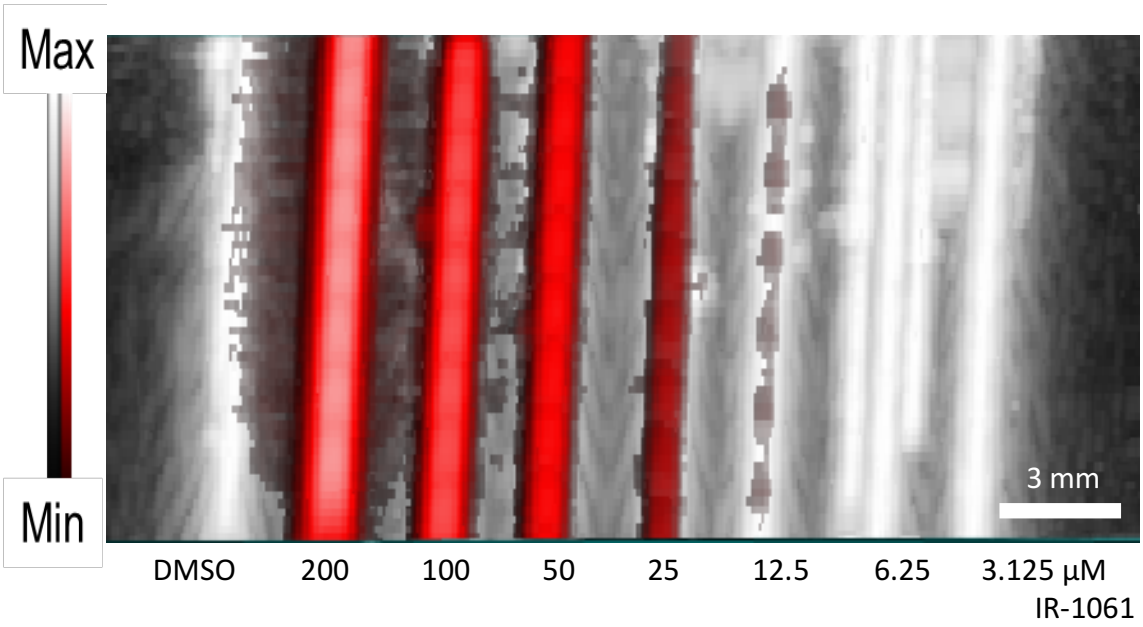

Figure 14: Photoacoustic imaging of free IR-1061 at 200, 100, 50, 25, 12.5, 6.25, 3.125 μM in DMSO.

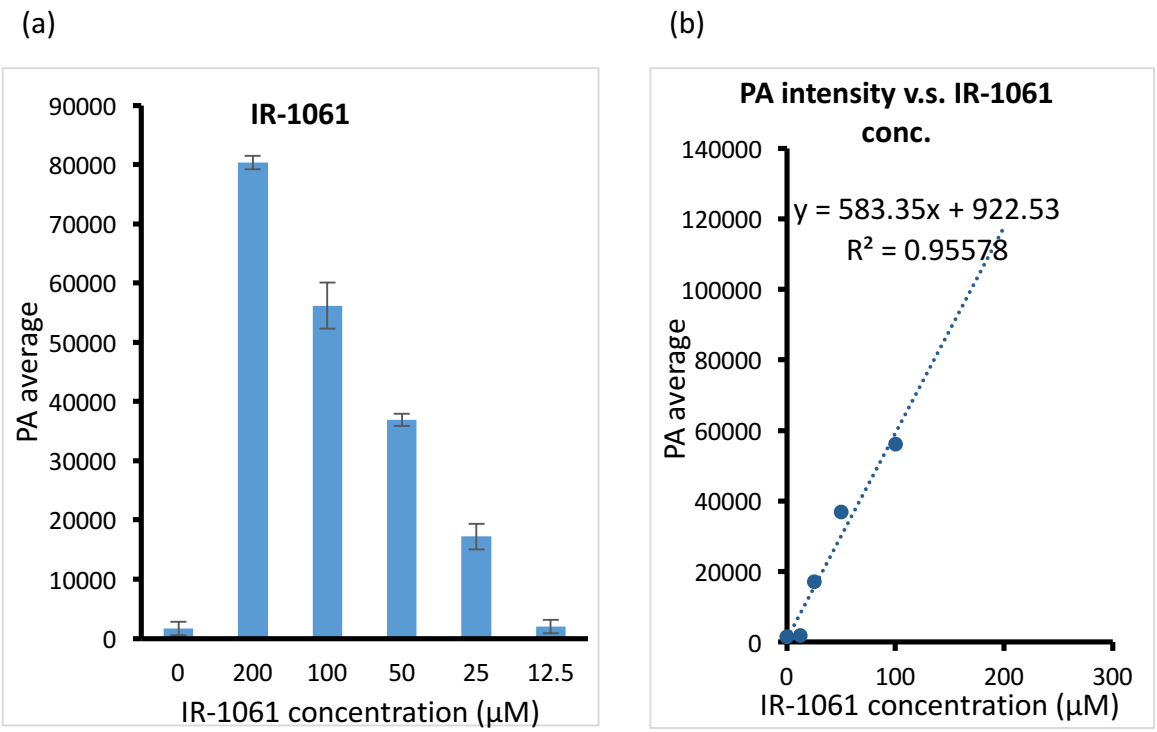

Figure 15: Quantification of photoacoustic intensity from free IR-1061 at different concentrations in DMSO. (a) PA average intensity of IR-1061 at 200, 100, 50, 25, 12.5 μM in DMSO. (b) Standard line of photoacoustic intensity against IR-1061 at 200, 100, 50, 25, 12.5 μM in DMSO.

(2) IR-1061-loaded hybrid nanoparticles:

The photoacoustic imaging of IR-1061-loaded nanoparticles are illustrated in Figure 16. Combined with Table 5, it was obvious that the photoacoustic signals came from IR-1061 since PBS and nanoparticles without IR-1061 did not have signals in the image. However, the nanoparticles loaded with IR-1061 less than 50 μM also have no photoacoustic signals. When IR-1061 molecules were loaded into nanoparticles, it was highly likely that the locally high concentration of IR-1061 may quench photoacoustic signals of itself. As a result, the nanoparticles loaded with IR-1061 at 25 μM showed no photoacoustic signal even though the concentration of IR-1061 is much higher than the detection limit (7.04 μM).

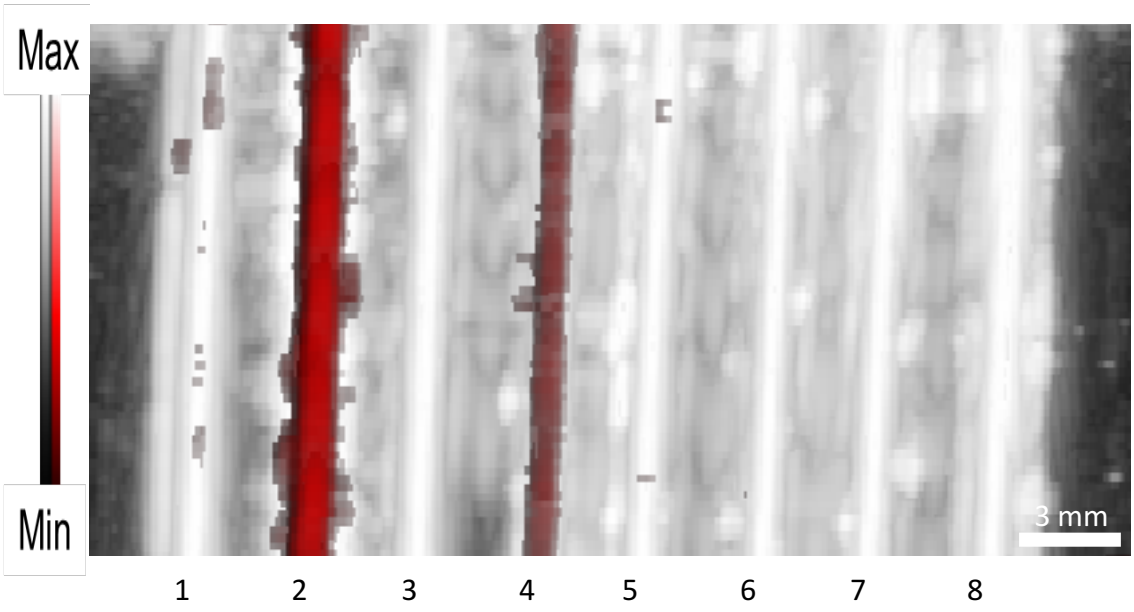

Figure 16: Photoacoustic imaging of IR-1061-loaded nanoparticles. The samples from left to right are 1: PBS, 2: NP w/IR-1061100 μM, 3: NP w/o IR-1061, 4: NP w/IR-1061 50 μM, 5: NP w/IR-1061 50μM, 6: NP w/IR-1061 12.5 μM, 7: NP w/IR-1061 6.25 μM, and 8: NP w/IR-10613.125 μM.

Table 5: Photoacoustic imaging of IR-1061-loaded nanoparticle samples.

index	sample
1	PBS
2	NP w/IR-1061 100 μM
3	NP w/o IR-1061
4	NP w/IR-1061 50 μM
5	NP w/IR-1061 25 μM
6	NP w/IR-1061 12.5 μM
7	NP w/IR-1061 6.25 μM
8	NP w/IR-1061 3.125 μM

(3) Photoacoustic Imaging of Release Samples:

We measured the photoacoustic intensity of all releasing samples. Figure 17 showed the photoacoustic imaging of IR-1061 released from our nanoparticles in PBS at different pH at 0.5h. The result corresponds to the release profile (Figure 12). As we expected, there were higher amount of IR-1061 released in PBS in more acidic environment. These higher amount of IR-1061 induced more thermos-elastic expansion effect and caused higher photoacoustic intensity in the imaging.

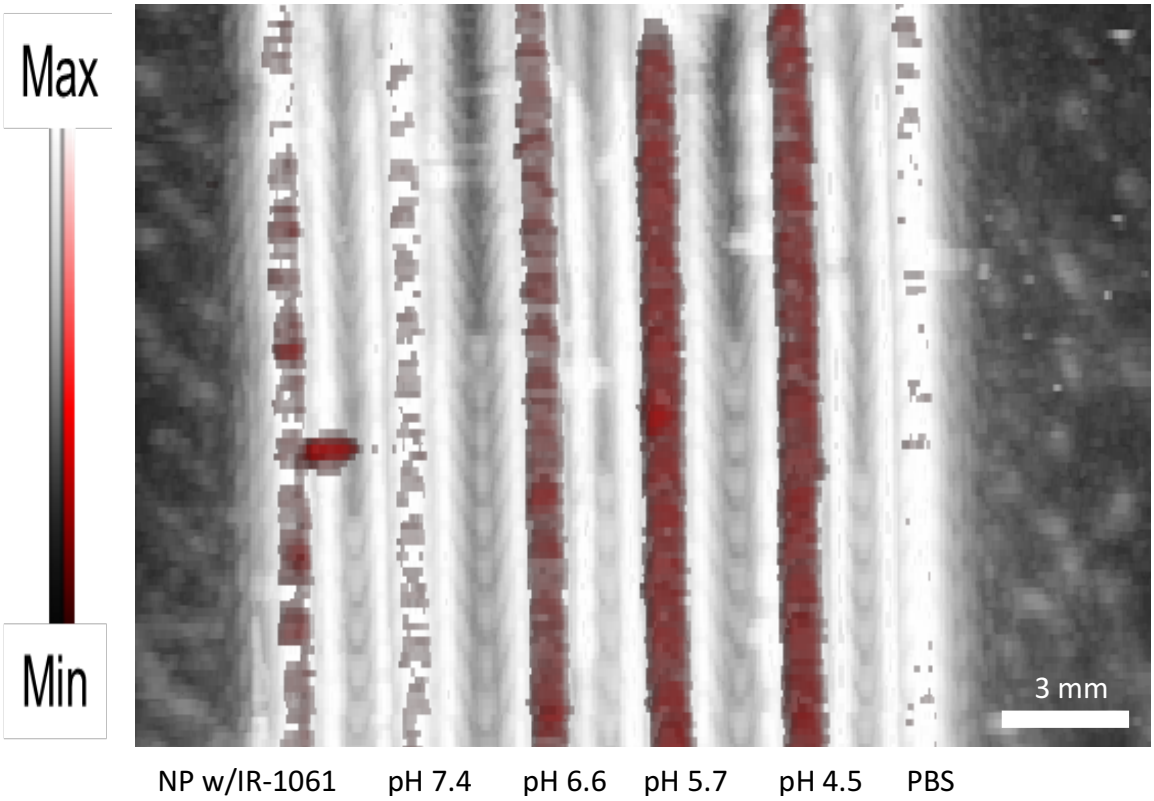

Figure 17: Photoacoustic imaging of IR-1061 released from hybrid nanoparticles in PBS at pH 7.4, 6.6, 5.7, 4.5 at 0.5h.

Discussion

1. Characterization of DiR- and IR-1061-loaded hybrid nanoparticles

In this study, we successfully developed DiR-loaded and IR-1061-loaded hybrid nanoparticles. The average size of DiR-loaded and IR-1061-loaded nanoparticles are around 200 nm and 130 nm, respectively, which is optimal for extravasation across premature and abnormal vasculature in tumor tissues[22]. So, our nanoparticles could passively accumulate in tumor tissues by enhanced permeability and retention (EPR) effect. It's rather reasonable that the size of our DiR- and IR-1061-loaded hybrid nanoparticles are both larger than PLGA nanoparticles (45.7 nm) because the extra PEG hydrophilic shell enlarges the average size of the hollow hybrid nanoparticles. Also, the encapsulated DiR and IR-1061 molecules further make the average size of the hybrid nanoparticles even larger. Besides, both DiR-loaded and IR-1061-loaded nanoparticles obtain around 70% of dye loading efficiency. DiR molecules were encapsulated in PLGA hydrophobic core by hydrophobic interactions while IR-1061 molecules were loaded into nanoparticles by hydrophobic interactions and electrostatic interactions. The high dye loading efficiency may be due to lipid-polymer interface. The interface around PLGA polymer can prevent diffusion of hydrophobic dye molecules out of nanoparticles and enhance the dye loading. Plus, the pronounced blue shift (absorbance peak at 1074 nm to 900 nm) absorbance spectrum occurred when IR-1061 molecules were loaded into nanoparticles. The blue shift may be due to the π-π stacking interactions between DiR and IR-1061 molecules when they aggregate in the PLGA hydrophobic core. This may change the electron resonance properties and ultimately result in blue shift of the

absorbance spectrum. This property made IR-1061 a potential candidate to combine with anticancer drugs and utilize in drug delivery.

2. Active targeting capability of DiR-loaded hybrid nanoparticles

To validate active targeting capability of our hybrid nanoparticles, we use anti-folate receptor antibodies to stain A549, HeLa, Ov2008, and SKOV3 cells. After immune-staining, A549 and HeLa cells were selected as folate receptor negative and positive cell lines because of the 1. 1-fold and 7.1-fold expression of folate receptors on their cell membrane, respectively. We co-incubated A549 and HeLa cells with our folate-functionalized nanoparticles loaded with DiR and used flow cytometer to track the cell uptake of our nanoparticles. It turned out that 95.8% of our folate-functionalized nanoparticles could be rapidly engulfed into HeLa cells in 0.5 h via receptor-mediated endocytosis. In contrast, A549 cells only nonspecifically engulfed 45.2% of our folate-functionalized nanoparticles in 0.5 h. Furthermore, we used folate pre-treatment to further confirm the active targeting capability of our folate-functionalized nanoparticles. After folate pre-treatment, HeLa cells showed dose-dependent decrease cell uptake of our folate-functionalized nanoparticles while A549 cells had no difference of their cell uptake. The dose-dependent decrease cell uptake of folate-functionalized nanoparticles in HeLa cells results from blocking of folate receptors on their cell membrane. On the other hand, blockage of folate receptors had little effect to the originally folate receptor-deficient A549 cells. As a result, we firmly validate the active targeting capability of our folate-functionalized nanoparticles. After passing through inter-endothelial junctions of

tumor vasculature, our nanoparticles can not only passively accumulate in tumor tissues but also be engulfed by tumor cells via folate receptor-mediated endocytosis.

3. Photoacoustic imaging and release profile of IR-1061-loaded hybrid nanoparticles

In photoacoustic imaging, we obtained the detection limit of IR-1061 in DMSO was 7.04 μM. However, when IR-1061 molecules were encapsulated into hybrid nanoparticles, it showed no photoacoustic signal even the IR-1061 was at 25 μM, which was 4 times higher than the detection limit. This may be due to the aggregation of IR-1061 molecules in the PLGA core. When IR-1061 molecules aggregate, they couldn't get irradiated efficiently to produce thermal expansion effect and acoustic wave, which ultimately results in weak photoacoustic signals. Then, our IR-1061-loaded nanoparticles were added to PBS at pH 7.4, 6.6, 5.7, and 4.5 to initiate the release experiment. We harvested the supernatant of each release sample at different time points. The supernatant samples were scanned by photoacoustic transducer. At all the time points, the more acidic the environment, the more IR-1061 get released. We speculated that the pH-responsive release profile stemmed from the positive charges on IR-1061 molecules. At lower pH, the protons disturb the electro-static interactions between negatively charged PLGA core and IR-1061 and lead to greater amount of IR-1061 release. The pH-responsive release profile was further validated by photoacoustic imaging. Similarly, the releasing samples in pH 4.5 and 5.7 obviously obtained stronger photoacoustic signals than in pH 6.6 and 7.4. Again, it's due to the greater amount IR-1061 released in more acidic PBS. However, the greater amount of released IR-1061 also caused more aggregates in

aqueous solution when release time went up to 24h. This is mainly due to hydrophobic nature of IR-1061. Although the increase amount of IR-1061 molecules released leads to strong photoacoustic signals in the beginning, the photoacoustic signals decay in the long run. It's due to the fact that IR-1061 molecules aggregate in PBS when they are released to some extent. In our long-term goal to track release profile of IR-1061-drug conjugates via photoacoustic imaging, we should chemically modify IR-1061 molecules and make more hydrophilic. Otherwise, the aggregation of IR-1061 would quench the photoacoustic signals in releasing samples and cause inaccurate quantification of released IR-1061 molecules.

Materials and Methods

1. Preparation of DiR-loaded hybrid nanoparticles

The hybrid nanoparticles we used in this research studies were made by nanoprecipitation method[21]. Briefly, prepare 1 mg/mL lecithin/ DSPE-PEG-folate (1,2-distearoyl-sn-glycero-3-phoshoethanolamine-N-carboxy(polyethylene glycol)5000-folate) mixed lipid solution and 1mg/mL PLGA (poly(D,L-lactic-co-glycolic acid)) solution. Lecithin and DSPE-PEG-folate (molar ratio 85/15) were dissolved in 4% (v/v) ethanol and PLGA polymers were dissolved in acetonitrile solution. Then, the PLGA solution was added dropwise into mixed lipid solution under gentle stirring. After adding PLGA solution, the whole solution was vortexed for 3 min and further stirred for 2h. Then, we used Ultra-4 centrifugal filter (Millipore, Billerica, MA) with molecular weight cutoff of 10,000 Da to harvest the nanoparticles by centrifuging the nanoparticle solution at 4000×g for 15 min. To make DiR (Biotrium)-loaded hybrid nanoparticles, DiR with optimal dosage was added to PLGA acetonitrile solution before the nanoprecipitation process. The size (diameter, nm) and the surface charge (ζ potential, mV) were measured by quasi-elastic laser light scattering with a ZetaPALS dynamic light scattering detector (Brookhaven Instruments Corporation, Holsville, NY).

2. Preparation of IR-1061-loaded hybrid nanoparticles

The hybrid nanoparticles we used in this research studies were made by nanoprecipitation method[20]. Briefly, prepare 1 mg/mL or 2 mg/mL lecithin/ DSPE-PEG-folate (1,2-distearoyl-sn-glycero-3-phoshoethanolamine-N-carboxy(polyethylene

glycol)5000-folate) mixed lipid solution and 1mg/mL PLGA (poly(D,L-lactic-co-glycolic acid)) solution. Lecithin and DSPE-PEG-folate (molar ratio 85/15) were dissolved in 4% (v/v) ethanol and PLGA polymers were dissolved in DMSO (dimethyl sulfoxide) solution. Then, the PLGA solution was added dropwise into mixed lipid solution under sonication. After adding PLGA solution, the whole solution was further sonicated for 5 min. Then, wash hybrid nanoparticles 5 times with an Amicon Ultra-4 centrifugal filter (Millipore, Billerica, MA) with molecular weight cutoff of 100,000 Da to remove the remaining DMSO solvent in the nanoparticle solution. To make DiR or IR-1061 loaded hybrid nanoparticles, DiR or IR-1061 with optimal dosage was added to PLGA DMSO solution before the nanoprecipitation process. The size (diameter, nm) and the surface charge (ζ potential, mV) were measured by quasi-elastic laser light scattering with a ZetaPALS dynamic light scattering detector (Brookhaven Instruments Corporation, Holsville, NY).

3. Dye loading and release study

To obtain the dye loading efficiency, 1 mL nanoparticle solution was lyophilized. Then, use the equivalent amount of DMSO to destroy nanoparticles and get the encapsulated DiR or IR-1061 released. The absorbance of DiR (at 765 nm) and IR-1061 (at 1074 nm) the solution was measured by plate reader or UV-VIS-NIR spectrophotometer. Combined with their standard line, we can calculate the amount of encapsulated DiR or IR-1061. Then, we can calculate the loading efficiency by using the following equation.

$$\text{Loading Efficiency} = \frac{the\ amount\ of\ encapsulated\ dye}{the\ amount\ of\ added\ dye} \times 100\%$$

In this study, we used IR-1061 loaded nanoparticles to do the release study. Briefly, 0.5 mL concentrated IR-161 loaded nanoparticles were harvested and added to 9.5 mL PBS at pH 7.4, 6.6, 5.7, and 4.5. The starting concentration of IR-1061 in nanoparticles was 15 μM. Then, we split the releasing solution at different pH into 10 microcentrifuge tubes (1 mL/ tube) and put them in 37 °C isothermal oven. All samples were kept rotating in isothermal oven via rotor to prevent precipitation of nanoparticles. Releasing samples were spun down (10,000×g, 20 min) at 0.5, 1, 2, 4, 8, 24, 48, 72, and 96h. We collected the supernatant of each sample and measured the absorbance and photoacoustic intensity by UV-VIS-NIR spectrophotometer and Vivo LAZR scanner, respectively.

4. Immunostaining of folate receptors

A549, HeLa, Ov2008, and SKOV3 cells were plated on 6-well tissue culture plate (250,000 cells/ well) and incubated for 24h. Remove the cell medium. Trypsinize cells and spin down cells at 1000 rpm for 5 min. Remove the supernatant and collect the cell pallets. Then, add 1 mL ice-cold PBS to resuspend the cells and start immunostaining by adding 3 μL primary antibodies. For control group, just add 3 μL of PBS instead of primary antibodies to compare the results. Then, incubate the cells for 1h on ice bath. After 1h incubation, remove the primary antibodies-containing cell medium and use PBS to wash cells 2 times. Then, resuspend the cells in ice-cold PBS. After resuspension, add 4 μL secondary antibodies to all cell samples including control group and incubate them on ice bath for another 1h. Finally, remove the antibodies-containing PBS, wash the cells

twice with ice-cold PBS, and resuspend the cells in ice-cold PBS. We use flow cytometer to examine the FITC signals in each cell line.

5. Cell uptake

The cell models we used in this study were A549 and HeLa cells to validate the active targeting capability of our folate-functionalized hybrid nanoparticles. A549 is a small cell lung cancer cell line which has deficient folate receptor expression on its' surface of cell membrane. In contrast, HeLa is a cervical cancer cell line which has folate receptor overexpression on the cell membrane. A549 and HeLa cells were plated on 6-well tissue culture plate (250,000 cells/ well) and incubated for 24h. Remove the RPMI cell medium. Then, add DiR-loaded hybrid nanoparticles to cell medium and incubate with cells for 0.5 and 1h. After incubation, remove the nanoparticle-containing cell medium and use PBS to wash cells 2 times. After washing, add 1 mL trypsin to trypsinize cells for 5 min. Then, add 2 mL RPMI cell medium and spin down (1000 rpm, 5 min) cells. Aspirate the medium and add 1 mL methanol to fix the cells for 10 min. Again, spin down (1000 rpm, 5 min) the cells and wash the cells 2 times to remove remaining methanol. After washing, re-suspend the cells with 1 mL PBS and put the cell solutions in ice-bath. Use flow cytometer to measure the DiR intensity of all samples. To further confirm the active targeting capability of our folate-functionalized nanoparticles. We did the folate competition experiment. Briefly, we added RPMI medium containing 1, 2, 4 mM folate to the wells for 1h prior to adding any DiR-loading nanoparticles. After folate pre-treatment, we followed the same process to examine the cell uptake of DiR-loaded nanoparticles.

6. Cell viability

A549 and HeLa cells were plated on 96-well plate (8000 cells/well) and incubated for 24h. Remove the cell medium and add 100 μL RPMI medium containing 200, 100, 50, 25, 12.5 μg/mL IR-1061- loaded nanoparticles and 70% ethanol to the wells. After 4h, remove the medium or ethanol and add 100 μL 10% MTT reagent to treat the cells for another 4h. Then, remove the MTT reagents and add 100 μL DMSO to dissolve the purple crystals. Use plate reader to measure the absorbance at 570 nm.

Conclusion

In this study, we successfully developed nanoparticle-based imaging agents which can be applied to in vivo imaging and ovarian cancer diagnosis. The size DiR-loaded and IR-1061-loaded nanoparticles are optimized for extravasation in tumor vasculature and able to passively accumulated in tumor tissues. The lipid-polymer interface in our hybrid nanoparticles promotes higher loading of DiR and IR-1061. The loading efficiency of these imaging agents could be as high as 70%. Moreover, our folate-functionalized nanoparticles with DiR could actively target to HeLa cells and be rapidly engulfed via receptor-mediated endocytosis in 0.5h. We even performed folate competition experiment to further validate the active targeting capability of our nanoparticles. Then, the release profile of IR-1061 loaded nanoparticles were examined. Obviously, it's a substaintial release profile with pH-responsive release tendency. The release of IR-1061 can reach around 60% in pH 4.5 PBS at 96h. Nonethelss, the hydrophobicity of IR-1061 cause severe aggregation after 24h and quenching of photoacoustic signals. Hence, we need to chemically modified the IR-1061 molecules and make it more hydrophilic in the future so that we can utilize photoacoustic imaging to accurately quantify the release of IR-1061-drug conjugates.

References

1. Jokerst, J. V.; Cole, A. J.; Van de Sompel, D.; Gambhir, S. S., Gold Nanorods for Ovarian Cancer Detection with Photoacoustic Imaging and Resection Guidance via Raman Imaging in Living Mice. *ACS Nano* **2012,** *6* (11), 10366-10377.

2. Jokerst, J. V.; Van de Sompel, D.; Bohndiek, S. E.; Gambhir, S. S., Cellulose nanoparticles are a biodegradable photoacoustic contrast agent for use in living mice. *Photoacoustics* **2014,** *2* (3), 119-127.

3. Lutz, A. M.; Willmann, J. K.; Drescher, C. W.; Ray, P.; Cochran, F. V.; Urban, N.; Gambhir, S. S., Early diagnosis of ovarian carcinoma: is a solution in sight? *Radiology* **2011,** *259* (2), 329-45.

4. Bast, R. C.; Hennessy, B.; Mills, G. B., The biology of ovarian cancer: new opportunities for translation. *Nat Rev Cancer* **2009,** *9* (6), 415-428.

5. Clarke-Pearson, D. L., Screening for Ovarian Cancer. *New England Journal of Medicine* **2009,** *361* (2), 170-177.

6. Menon, U.; Gentry-Maharaj, A.; Hallett, R.; Ryan, A.; Burnell, M.; Sharma, A.; Lewis, S.; Davies, S.; Philpott, S.; Lopes, A.; Godfrey, K.; Oram, D.; Herod, J.; Williamson, K.; Seif, M. W.; Scott, I.; Mould, T.; Woolas, R.; Murdoch, J.; Dobbs, S.; Amso, N. N.; Leeson, S.; Cruickshank, D.; McGuire, A.; Campbell, S.; Fallowfield, L.; Singh, N.; Dawnay, A.; Skates, S. J.; Parmar, M.; Jacobs, I., Sensitivity and specificity of multimodal and ultrasound screening for ovarian cancer, and stage distribution of detected cancers: results of the prevalence screen of the UK Collaborative Trial of Ovarian Cancer Screening (UKCTOCS). *The Lancet Oncology* **2009,** *10* (4), 327-340.

7. Bohndiek, S. E.; Wagadarikar, A.; Zavaleta, C. L.; Van de Sompel, D.; Garai, E.; Jokerst, J. V.; Yazdanfar, S.; Gambhir, S. S., A small animal Raman instrument for rapid, wide-area, spectroscopic imaging. *Proceedings of the National Academy of Sciences of the United States of America* **2013,** *110* (30), 12408-12413.

8. Jun Liu and Jie Li and Thomas, J. R. a. X. P. a. J. L. V., Biodegradable nanoparticles for targeted ultrasound imaging of breast cancer cells in vitro. *Physics in Medicine and Biology* **2007,** *52* (16), 4739.

9. Pu, K.; Shuhendler, A. J.; Jokerst, J. V.; Mei, J.; Gambhir, S. S.; Bao, Z.; Rao, J., Semiconducting polymer nanoparticles as photoacoustic molecular imaging probes in living mice. *Nat Nano* **2014,** *9* (3), 233-239.

10. Jokerst, J. V.; Khademi, C.; Gambhir, S. S., Intracellular Aggregation of Multimodal Silica Nanoparticles for Ultrasound-Guided Stem Cell Implantation. *Science Translational Medicine* **2013,** *5* (177), 177ra35.

11. Kircher, M. F.; de la Zerda, A.; Jokerst, J. V.; Zavaleta, C. L.; Kempen, P. J.; Mittra, E.; Pitter, K.; Huang, R.; Campos, C.; Habte, F.; Sinclair, R.; Brennan, C. W.; Mellinghoff, I. K.; Holland, E. C.; Gambhir, S. S., A brain tumor molecular imaging strategy using a new triple-modality MRI-photoacoustic-Raman nanoparticle. *Nat Med* **2012,** *18* (5), 829-834.

12. Jokerst, J. V.; Thangaraj, M.; Kempen, P. J.; Sinclair, R.; Gambhir, S. S., Photoacoustic Imaging of Mesenchymal Stem Cells in Living Mice via Silica-Coated Gold Nanorods. *ACS Nano* **2012,** *6* (7), 5920-5930.

13. Yun, S. H.; Kwok, S. J. J., Light in diagnosis, therapy and surgery. *Nature Biomedical Engineering* **2017,** *1*, 0008.

14. Hong, G.; Antaris, A. L.; Dai, H., Near-infrared fluorophores for biomedical imaging. *Nature Biomedical Engineering* **2017,** *1*, 0010.

15. Diao, S.; Blackburn, J. L.; Hong, G.; Antaris, A. L.; Chang, J.; Wu, J. Z.; Zhang, B.; Cheng, K.; Kuo, C. J.; Dai, H., Fluorescence Imaging In Vivo at Wavelengths beyond 1500 nm. *Angewandte Chemie International Edition* **2015,** *54* (49), 14758-14762.

16. Antaris, A. L.; Chen, H.; Cheng, K.; Sun, Y.; Hong, G.; Qu, C.; Diao, S.; Deng, Z.; Hu, X.; Zhang, B.; Zhang, X.; Yaghi, O. K.; Alamparambil, Z. R.; Hong, X.; Cheng, Z.; Dai, H., A small-molecule dye for NIR-II imaging. *Nat Mater* **2016,** *15* (2), 235-242.

17. Hong, G.; Lee, J. C.; Robinson, J. T.; Raaz, U.; Xie, L.; Huang, N. F.; Cooke, J. P.; Dai, H., Multifunctional in vivo vascular imaging using near-infrared II fluorescence. *Nat Med* **2012,** *18* (12), 1841-1846.

18. Welsher, K.; Sherlock, S. P.; Dai, H., Deep-tissue anatomical imaging of mice using carbon nanotube fluorophores in the second near-infrared window. *Proceedings of the National Academy of Sciences* **2011,** *108* (22), 8943-8948.

19. Texier, I.; Goutayer, M.; Da Silva, A.; Guyon, L.; Djaker, N.; Josserand, V.; Neumann, E.; Bibette, J.; Vinet, F., Cyanine-loaded lipid nanoparticles for improved in vivo fluorescence imaging. *Journal of Biomedical Optics* **2009,** *14* (5), 054005-054005-11.

20. Tao, Z.; Hong, G.; Shinji, C.; Chen, C.; Diao, S.; Antaris, A. L.; Zhang, B.; Zou, Y.; Dai, H., Biological imaging using nanoparticles of small organic molecules with fluorescence emission at wavelengths longer than 1000 nm. *Angew Chem Int Ed Engl* **2013,** *52* (49), 13002-6.

21. Zhang, L.; Chan, J. M.; Gu, F. X.; Rhee, J.-W.; Wang, A. Z.; Radovic-Moreno, A. F.; Alexis, F.; Langer, R.; Farokhzad, O. C., Self-Assembled Lipid−Polymer Hybrid Nanoparticles: A Robust Drug Delivery Platform. *ACS Nano* **2008,** *2* (8), 1696-1702.

22. Blanco, E.; Shen, H.; Ferrari, M., Principles of nanoparticle design for overcoming biological barriers to drug delivery. *Nat Biotech* **2015,** *33* (9), 941-951.